Numerical Study of Nanosecond Pulsed Laser Impact on a Water Droplet

Zhenyu Zhao* and Weizhong Li†

Key Laboratory of Ocean Energy Utilization and Energy Conservation of Ministry of Education, Dalian University of Technology, Dalian 116024, China

(Received 26 November 2020; revised 16 May 2021; accepted 23 June 2021; published 16 July 2021)

An integrated hydrodynamic model that involves a laser heat source, surface evaporation, and interfacial driving forces is developed to simulate the complex physical process of a nanosecond pulsed laser impacting on a water droplet. Droplet deformation tracked by the coupled level set and volume of fluid method is contrasted with the experimental results, and it is shown that the coupled model can be used to simulate the droplet expansion dynamics. From the simulation of droplet deformation, it can be found that, with increasing laser energy, the droplet becomes thinner. With the highest laser energy, the jet on the opposite side to laser impact is interpreted as the flow of high-speed fluid near the axis, which is also confirmed by the velocity field. The simulated temperature reaches or even exceeds the critical value, and the recoil pressure does not completely cover the whole hemispherical surface of the droplet. The liquid-removal depth, which represents the distance that the liquid-phase interface retreats during evaporation, is much shallower than the absorption depth. It can be concluded that propulsion is gained from the intense evaporation of the superheated layer.

DOI: 10.1103/PhysRevApplied.16.014042

I. INTRODUCTION

Upon pulsed laser ablation on a droplet, energy is deposited on a thin layer of the surface. The focused energy will cause a dramatic temperature rise, followed by violent vaporization, explosive boiling, and even plasma for liquid metal, which could result in a strong recoil pressure that propels the droplet to expand, deform, and even fragment [1].

The droplet dynamics under the impact of a pulsed laser beam are of great significance to the laser-produced plasma light source in extreme ultraviolet (EUV) lithography. EUV lithography is considered as a promising technology to ensure high resolution below 10 nm for next-generation semiconductor manufacturing. A liquid-tin droplet as a target is first irradiated by a prepulse laser to become a thin sheet and then by a main pulse laser to emit in the extreme ultraviolet region [2,3]. The dynamics of deformation and instability of the droplet need to be studied for precise control, so that the conversion efficiency (CE) is maximal [4,5].

The EUV light source is produced by a metal droplet irradiated with a pulsed laser and emits extreme ultraviolet light. The mechanism of interaction between the laser and liquid-metal droplet is very complex, especially when the pulse duration of the laser is shortened to picoseconds and even femtoseconds [6]. In fundamental research, it is necessary to choose a relatively simple case, that is, nanosecond pulsed laser interaction on a water droplet, which has not been investigated completely, and the mechanism needs to be much deeper understood. In the water-droplet case, there is no need to consider non-Fourier heat conduction and plasma formation. However, it is still a great challenge to understand the mechanism thoroughly.

Pulsed laser-induced propulsion and strong deformation of water droplets are studied experimentally [7]. The droplets are dyed, which ensures that the laser energy is limited to a superficial layer of the drop and leads to a more violent response [8]. A liquid indium-tin microdroplet impacted by the propulsion of a nanosecond pulse laser is also investigated experimentally [9]. Laser ablations of water droplets and liquid-metal droplets represent two experimental systems. The differences in propulsion mechanisms between the two systems are extensively investigated [10].

If the pulse width of the laser is shortened to picoseconds or femtoseconds, the physical mechanisms become more complex. The study of droplet deformation with femtosecond and picosecond pulsed lasers demonstrate that liquid compressibility should be taken into account practically [11]. In the regime where the Mach number is much greater than one, more complex mechanisms will be involved, such as shock waves, cavitation, nonlinear viscous damping, and rapid interface acceleration, which lead

*eduzhao@mail.dlut.edu.cn
†wzhongli@dlut.edu.cn

to linear-model breakdown. It is also reported that cavitation results in the droplet center when it is irradiated by an ultrashort pulsed laser due to the shock wave and rarefaction wave [12]. Additionally, explosions brought by x-ray free-electron lasers on water drops and jets are modeled, and liquid and vapor dynamics are investigated [13,14]. The ultrafast (duration 30 fs) deposition of high energy densities (photon energy of several keV) can make matter under extreme conditions.

Simulations of laser impact on materials are widely studied, such as in pulsed laser deposition, laser welding, and laser drilling [15,16]. Sawyer *et al.* [17] presented laser thermal ablation modeling that combined optical coupling, heat flow, melt flow due to recoil pressure, evaporation, and gas dynamics in a coupled multiphysics model. Ai *et al.* [18] proposed three-dimensional numerical simulation modeling to investigate keyhole profile characteristics and the effect of keyhole evolution on the molten pool during laser welding. Zhang *et al.* [19] developed a modified level-set method to simulate the laser drilling process on an aluminum slab.

There are plenty of numerical simulations to study laser ablation on a planar surface, as mentioned above, but there are few studies on a droplet. The mechanism of laser impact on a droplet is not fully understood. Gelderblom *et al.* [20] applied a Gaussian-shaped pressure boundary condition on the droplet surface for simplicity with a boundary integral (BI) simulation. Because the evaporation process is not considered, the total process is analyzed with the help of the time-scaling law. Using a pressure boundary condition to simulate droplet deformation cannot reflect the influence of laser energy and heat and mass transfer on temperature and pressure distributions and droplet deformation. As laser ablation of materials is a multiphysics coupling process, an integrated model will lead to a more accurate description than a method in which only pressure boundary conditions are applied on the droplet's surface.

The laser heat-source model and modeling of heat and mass transfer are the keys to studying laser ablation materials by numerical simulation. The laser heat-source model can be classified into surface heat source [21] and volumetric heat source [22,23]. During evaporation, the liquid phase changes into the gas phase, which causes mass transfer, and the evaporated particles take away heat, which leads to a decrease of the liquid-phase temperature. The Rankine-Hugoniot jump condition and Schrage model limit mass transfer at the interface, whereas the Lee model allows for phase changes both along the interface and within the saturated phase [24].

Here, a coupled numerical model, including the laser heat source, surface evaporation, and interfacial driving force models, is developed to study nanosecond pulsed laser impact on a water droplet. The laser intensity is in the range that can cause strong evaporation on the droplet surface but does not generate plasma. A volumetric heat source that describes laser deposition at a penetration depth on the illuminated side of the droplet is proposed and validated through a comparison of surface temperatures on the droplet between simulated and analytical results. Heat loss due to evaporation is taken into account. The surface tension and recoil pressure are considered as interfacial driving forces. The coupled level set and volume of fluid (CLSVOF) method is employed for interface tracking, and the simulation results are compared with experimental images. The mechanism of a jet phenomenon at the droplet surface is mainly discussed. Spatial temperature and pressure evolution are analyzed in detail. Finally, the liquid-removal depth is defined and computed in the simulation, with the aim of revealing the mechanism of heat and mass transfer during laser ablation of a water droplet.

II. MATHEMATICAL MODEL

A. Governing equations

A two-phase flow that is assumed to be incompressible and laminar, the liquid phase and the gas phase, is adopted to simulate laser-induced water-droplet deformation in ambient air. To reduce the complexity of the problem, assumptions are made for simplicity. Gravity is ignored and heat radiation is not considered. Evaporation that occurs at the interface is not treated as the Knudsen layer.

The governing equations for the conservation of mass (continuity), momentum, and energy are as follows:

$$\frac{\partial \rho}{\partial t} + \nabla(\rho \mathbf{U}) = 0, \tag{1}$$

$$\frac{\partial(\rho \mathbf{U})}{\partial t} + \nabla(\rho \mathbf{U}\mathbf{U}) = -\nabla p + \nabla[\mu(\nabla \mathbf{U} + \nabla \mathbf{U}^T)] + F_\sigma + F_{\text{recoil}}, \tag{2}$$

$$\rho c_p \left[\frac{\partial(T)}{\partial t} + (\mathbf{U} \cdot \nabla)T\right] = \nabla(k \nabla T) + S, \tag{3}$$

$$S = W_{\text{las}} - W_{\text{vap}}, \tag{4}$$

where ρ is the density, $\mathbf{U}$ is the velocity vector, p is the pressure, μ is the dynamic viscosity, C_p is the specific heat, k is the thermal conductivity, S is the heat source, F_σ is the surface-tension force and F_{recoil} is the recoil pressure. W_{las} and W_{vap} are the laser heat source and heat loss through evaporation, respectively. In this study, evaporation occurs only at the droplet surface irradiated by the laser and results in a recoil pressure on the droplet surface.

B. Tracking of droplet interface

The level-set method, as well as the volume of fluid (VOF) method, is a popular interface-tracking method for computing two-phase flows. Both methods can be used

to track the interfacial deformation in laser ablation of materials.

The level-set function, φ, is defined as a set distance to the interface. Accordingly, the interface is the zero level set, and the level-set function, φ, can be expressed as [25]

$$\phi(x,t) = \begin{cases} +|d| & \text{in the primary phase,} \\ 0 & \text{at the interface,} \\ -|d| & \text{in the secondary phase,} \end{cases} \tag{5}$$

where d is the distance from the interface.

The evolution of the level-set function is solved by

$$\frac{\partial \phi}{\partial t} + \nabla(\mathbf{U}\phi) = 0. \tag{6}$$

In the VOF method, a color function between zero and one, known as the volume fraction is used to distinguish between two different fluids. The volume fraction, f, in a control volume is defined as [26]

$$\begin{cases} f = 1 & \text{filled with the primary phase,} \\ f = 0 & \text{filled with the secondary phase,} \\ 0 < f < 1 & \text{at the interface.} \end{cases} \tag{7}$$

Because the level-set function is smooth and continuous, interface curvature and the surface-tension force can be accurately calculated. However, the level-set method is found to lack volume conservation [27]. The VOF method is naturally volume conserving, while the VOF function is discontinuous across the interface [25]. To overcome the deficiencies of the level-set method and the VOF method, the CLSVOF method is employed.

To maintain the level-set function as a set distance function, a reinitialization process is required for each time step [28]. The values of the VOF and the level-set function are both used to reconstruct the interface. In other words, the VOF method is used to capture the interface, and the gradient of the level-set function determines the curvature and the normal of the interface [29]. The VOF function is also solved by

$$\frac{\partial f}{\partial t} + \nabla(f\,\mathbf{U}) = 0, \tag{8}$$

where f is the volume fraction.

C. Laser heat-source model

Laser absorption at the target obeys the Beer-Lambert law [30]. The problem is solved in polar coordinates because the circular surface is then transformed into rectangular coordinates. Because laser radiation can be absorbed only in the local normal direction, the laser intensity should multiply the cosine of the incident angle,

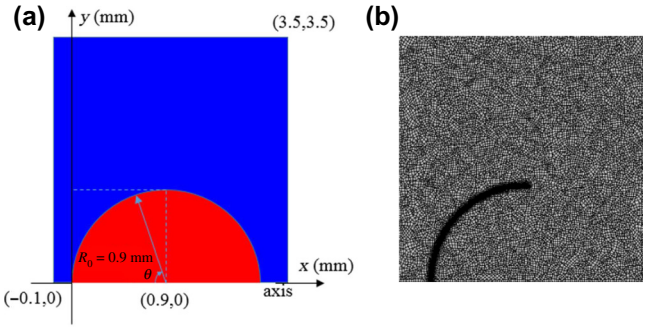

FIG. 1. (a) Computational domain; (b) meshing.

which equals the central angle corresponding to the droplet center. The source term of laser heat is expressed as

$$W_{\text{las}} = \alpha I_0 \cos\theta \exp\left\{-\alpha\left[R_0 - \sqrt{(x-R_0)^2 + y^2}\right]\right\}, \tag{9}$$

where α is the absorption coefficient, I_0 is the laser intensity, $R_0 = 0.9$ mm is the droplet radius, and

$$\cos\theta = \frac{R_0 - x}{\sqrt{(R_0 - x)^2 + y^2}}, \tag{10}$$

The schematic of the coordinates is depicted in Fig. 1. Considering heat loss taken by vaporization at the interface, the evaporation energy source term is

$$W_{\text{vap}} = m_{\text{vap}} L_{\text{v}}, \tag{11}$$

where m_{vap} is the evaporation mass rate (kg/s m^3) and L_{v} is the latent heat of evaporation (J/kg).

The parameters of a laser beam are shown in Table I, and the laser intensities for case 1–case 4 are listed in Table II, which corresponds to the actually absorbed laser energies in the experiment [7].

D. Surface-evaporation model

P_{sat} is the temperature-dependent saturation vapor pressure, which is derived from the integration of the Clausius-Clapeyron equation, and is expressed as follows:

$$p_{\text{sat}} = p_0 \exp\left[\frac{L_v}{R}\left(\frac{1}{T_b} - \frac{1}{T}\right)\right], \tag{12}$$

TABLE I. Laser-beam parameters.

Nd-YAG laser	Wavelength (nm)	Pulse duration (ns)	Spot size (mm)
Symbol	λ	τ_{laser}	D
	532	10	3.6

TABLE II. Laser intensity in the simulation and energy in the experiment.

	Case 1	Case 2	Case 3	Case 4
Laser intensity I_0 (W/m^2)	8.14×10^{11}	1.36×10^{12}	1.85×10^{12}	2.96×10^{12}
Energy (mJ)	6.6	11	15	24

where p_0 is the ambient pressure, T_b is the boiling temperature, and $R = 8.314$ J/mol K is the universal gas constant. The flow rate of mass transfer through the interface (kg/s m^2) is defined as [31]

$$\dot{m}_{\text{vap}} = p_{\text{sat}} \sqrt{\frac{m_a}{2\pi k_B T}}, \tag{13}$$

where $m_a = 3 \times 10^{-26}$ kg is the molecular mass of water and $k_B = 1.38 \times 10^{-23}$ J/K is the Boltzmann constant. Therefore, mass transfer caused by evaporation takes place at the interface of the liquid and gas phases.

The mass flow rate derived from the Hertz-Knudsen equation is the flow rate per unit area, and if it is multiplied by the interfacial area density, the flow rate per unit volume will be obtained (kg/s m^3):

$$m_{\text{vap}} = \dot{m}_{\text{vap}} A = p_{\text{sat}} \sqrt{\frac{m_a}{2\pi k_B T}} |\nabla f|, \tag{14}$$

where A is the interfacial area density, which is defined as the interfacial area between two phases per unit mixture volume (m^{-1}). This is an important parameter for predicting mass and energy transfer through the interface. Mass transfer at the interface per unit area should be converted into volumetric mass flux through the volume-fraction gradient of the gas phase, which requires a preexisting interface.

E. Interfacial-driving-force model

The main interfacial forces are surface tension and recoil pressure. The surface-tension force in the CLSVOF method is given by

$$F_\sigma = \sigma \kappa \delta(\phi) \hat{n}, \tag{15}$$

where σ is the surface-tension coefficient, $\hat{n}$ is local interface normal, κ is the local mean-interface curvature,

$$\hat{n} = \frac{\nabla \phi}{|\nabla \phi|}, \tag{16}$$

$$\kappa = \nabla \frac{\nabla \phi}{|\nabla \phi|}, \tag{17}$$

and

$$\begin{aligned} \delta(\phi) &= 0 && |\phi| \geq a, \\ \delta(\phi) &= \frac{1 + \cos(\pi \phi / a)}{2a} && |\phi| < a, \end{aligned} \tag{18}$$

where a is the thickness of the interface.

If the evaporated particles' return to the liquid phase is considered, a coefficient should be multiplied for intense evaporation, and the recoil pressure is [32]

$$p_{\text{recoil}} = 0.55 p_{\text{sat}} = 0.55 p_0 exp \left[\frac{L_v}{R} \left(\frac{1}{T_b} - \frac{1}{T} \right) \right]. \tag{19}$$

The interfacial recoil pressure is

$$f_{\text{recoil}} = p_{\text{recoil}} \hat{n}. \tag{20}$$

This interfacial force should be converted into volumetric force using the divergence theorem by multiplying it by a delta function Δ,

$$F_{\text{recoil}} = f_{\text{recoil}} \Delta, \tag{21}$$

where

$$\Delta = |\nabla f| \frac{2\bar{\rho}}{\rho_1 + \rho_2}, \tag{22}$$

and

$$\bar{\rho} = f_1 \rho_1 + f_2 \rho_2, \tag{23}$$

is the volume-averaged density, where ρ_1 and ρ_2 are the densities of the liquid and gas phases, respectively.

F. Liquid-removal-depth model

The coupled level set and VOF method is specifically designed for two-phase flows, where no mass transfer is involved, so a liquid-removal depth caused by evaporation is proposed. Interfacial mass transfer determined by Eq. (13) is used only to calculate heat loss due to evaporation. Because of material removal of the liquid phase, the interface will recede towards the liquid phase. The liquid-removal depth represents the interface recession that is not influenced by recoil pressure. The recession velocity can be expressed as

$$v_{\text{rec}} = \frac{\dot{m}_{\text{vap}}}{\rho_1} = \frac{p_{\text{sat}}}{\rho_1} \sqrt{\frac{m_a}{2\pi k_B T}}, \tag{24}$$

The liquid-removal depth, d, is the time integral of the recession velocity during the process of evaporation:

$$d = \int_{\tau_b}^{\tau_{b'}} v_{\text{rec}}(t) dt \quad (\tau_b \leq t \leq \tau_{b'}), \tag{25}$$

where τ_b and $\tau_{b'}$ are the times when evaporation starts and ends, respectively.

TABLE III. Physical properties of materials in the simulation.

Parameter	Water	Air
Density ρ (kg/m^3)	998	1.225
Boiling temperature T_b (K)	373	—
Critical temperature T_c (K)	647	—
Critical pressure P_c (MPa)	22.1	—
Specific heat C_p (J/kg K)	4190	1006
Thermal conductivity k (W/m K)	0.6	0.025
Latent heat of vaporization L_v (J/kg)	2.256×10^6	—
Molecular weight M (g/mol)	18	29
Dynamic viscosity μ [33] (N s/m^2)	$\mu = \mu_0 B\left[(a + a_1 T)p + (a_2 - a_3 T)p^2 + \frac{E - (b + b_1 T)p}{R(T - \theta - (c + c_1 T)p)}\right]$	1.22×10^{-6}
Surface tension coefficient σ [34] (N/m)	$\sigma = B\left(\frac{T_c - T}{T_c}\right)^{1.26}\left[1 + b\left(\frac{T_c - T}{T_c}\right)\right]$	—
Absorption coefficient α (m^{-1})	1×10^5	—

G. Numerical method

The computational domain is axisymmetric and rectangular with a size of 3.5×3.5 mm^2, as shown in Fig. 1(a), and boundary conditions are all pressure outlets except for the axis. It is also a multiscale problem because the droplet radius is 0.9 mm, while the energy-deposition depth is 10 μm. The meshes are refined near the droplet surface where it is irradiated by a laser, as illustrated in Fig. 1(b), to solve this problem.

Here, the governing equations are discretized by the finite-volume method and solved numerically in ANSYS FLUENT 16.0. The momentum and heat-source terms are implemented through user-defined functions. The physical properties of materials are listed in Table III.

III. RESULTS AND DISCUSSION

A. Surface-temperature validation

Temperature is a key parameter that determines the physical process and is dependent on the laser heat source. To verify the correctness of the numerical method, especially for the fineness of the grids, a one-dimensional theoretical model is proposed to help us better understand the laser-deposition mechanism and find out the relationships between the laser-beam profile and surface temperature.

If not considering heat loss due to evaporation and conductivity, laser energy deposited at the surface is all for increasing the internal energy of the liquid as follows:

$$c_p \rho x \Delta T = E_{\text{laser}} = \tau_{\text{laser}} \int_0^x \alpha I_0 e^{-\alpha x} dx, \tag{26}$$

$$\Delta T|_{x=0} = \lim_{x \to 0} \frac{\tau_{\text{laser}} I_0 (1 - e^{-\alpha x})}{c_p \rho x} = \frac{\alpha \tau_{\text{laser}} I_0}{c_p \rho}. \tag{27}$$

The analytical solution of temperature at the end of the pulse at the surface where $x = 0$ is obtained:

$$T_s = \Delta T|_{x=0} + T_0, \tag{28}$$

where T_s is the maximum temperature of the droplet surface at (0,0) and $T_0 = 300$ K is the initial temperature. To testify that the laser heat-source model is accurate, the simulated surface temperature without an evaporation-energy source term is compared with the analytical result, as shown in Fig. 2. $I_0 = 3.7 \times 10^{11}$ W/m^2 is the evaporation threshold, which corresponds to the absorbed energy of 3.3 mJ measured in the experiment. It can be seen that the simulation results are in good agreement with the analytical solutions.

Laser energies are determined by heating the superficial layer to boiling temperature but without vaporizing all of it [7]. From both the analytical and simulation results, it can be found that the surface temperature far exceeds the boiling point and even reaches or exceeds the critical point of water because the characteristics of laser-deposition depth are considered in our model.

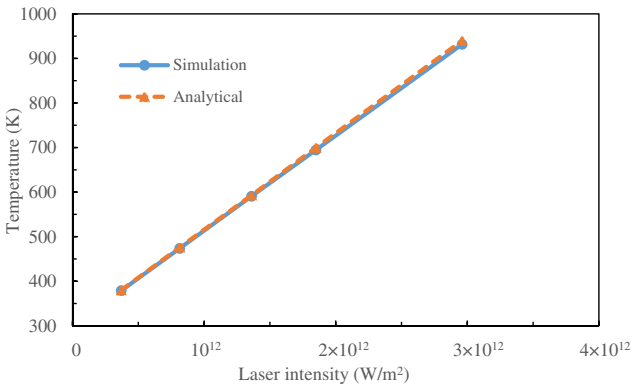

FIG. 2. Analytical and simulation results of maximum temperature at the surface.

B. Droplet deformation

Droplet deformation obtained by the simulation is depicted in Fig. 3. Because of the high laser energy close to the axis, the droplets become curved finally. As can be seen from the simulation results, the greater the power is, the thinner the droplets become under the recoil pressure. In case 4, the droplet is deformed into a curved thin sheet, which is the same as observed in the experiment. In the early stage, a crater is formed in the center of the droplet surface which cannot be seen in the experimental images in case 2–case 4. At a later time, the crater will merge into the droplet during deformation.

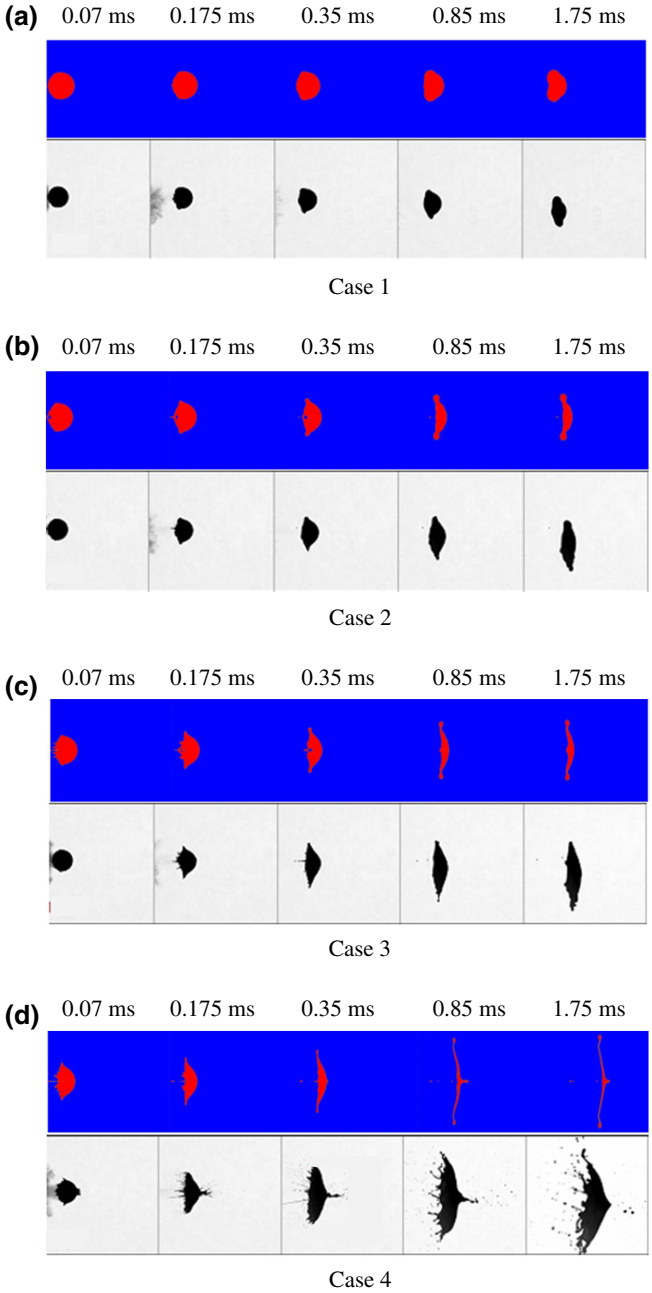

FIG. 3. Comparisons of water-droplet deformation in simulations (upper row) with experimental images (lower row).

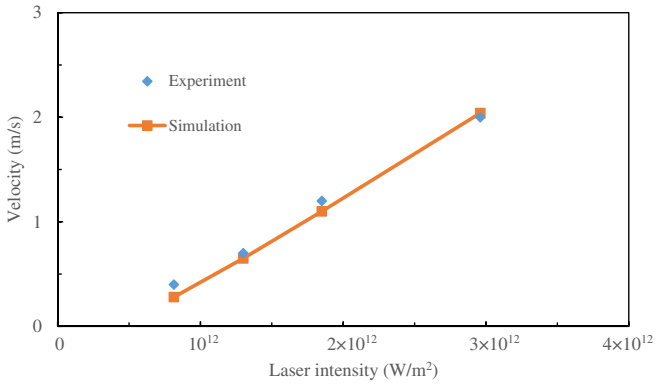

FIG. 4. Axial speed of water droplet as a function of laser intensity in experiment and simulations.

The axial droplet speed and radial expansion are compared with experimental results [7] in Figs. 4 and 5. In the studied laser intensities, the propulsion speed of droplets is proportional to the laser energy. With an increase of laser energy, the radial expansion of droplets becomes larger, up to fragmentation of the droplet's edge, as in case 4. The radial expansion of the droplet in the simulation results is consistent with experimental measurements. However, it can be found that the simulated values of droplet radial expansion are smaller than the experimental values. For the laser energy absorbed by the droplet, due to errors in the experimental measurements, the value measured by the energy meter is lower than that of energy actually absorbed. In addition, there are also some errors in the numerical iterations. These are possible reasons why the simulated values of radial expansion are smaller than the experimental values.

The jetting phenomenon opposite to the illuminated side can be observed in simulation results in case 4. It starts at 0.35 ms, but happens earlier in the experiment at 0.175 ms.

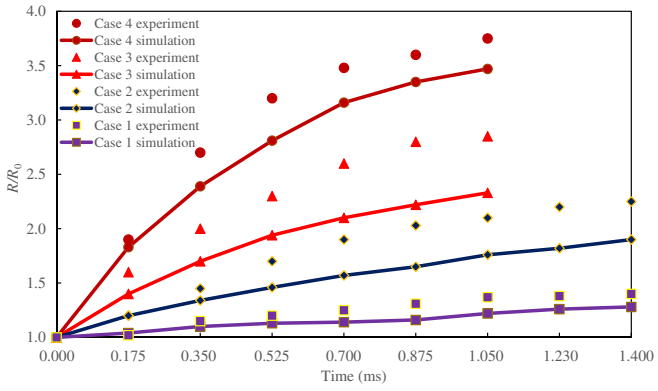

FIG. 5. Radial expansion of water droplets in experiment and simulations.

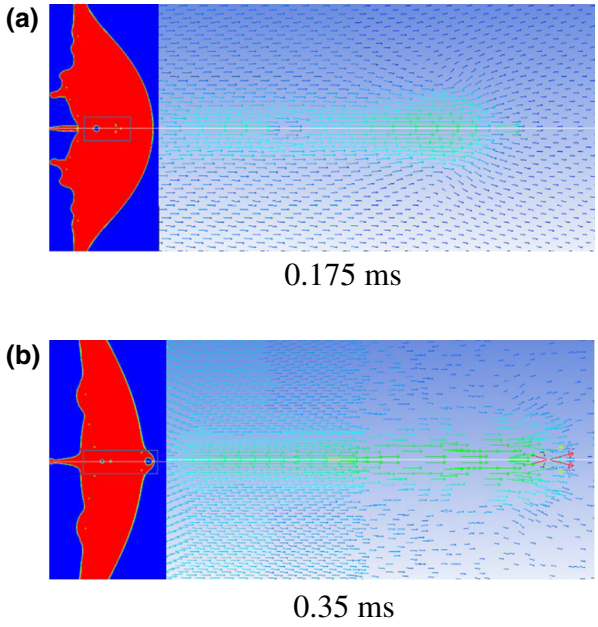

FIG. 6. Velocity fields of deformed droplet in case 4.

It develops until 0.85 ms and retracts at a later time due to the surface-tension effect. As we can see from Fig. 3, the deformed droplet becomes thinner with higher laser intensity, owing to increased recoil pressure. Due to the high power density in the center of the laser beam, the recoil pressure is also significantly greater than that in the adjacent area, which causes a crater to be formed at the axis where the fluid velocity along the axis is also much faster. With a higher laser intensity, the high-speed fluid has a greater opportunity to rush out from the droplet's surface until the liquid sheet is thin enough to form a jet. The velocity vectors of the deformed droplet at 0.175 and 0.35 ms are demonstrated in Fig. 6, which indicates

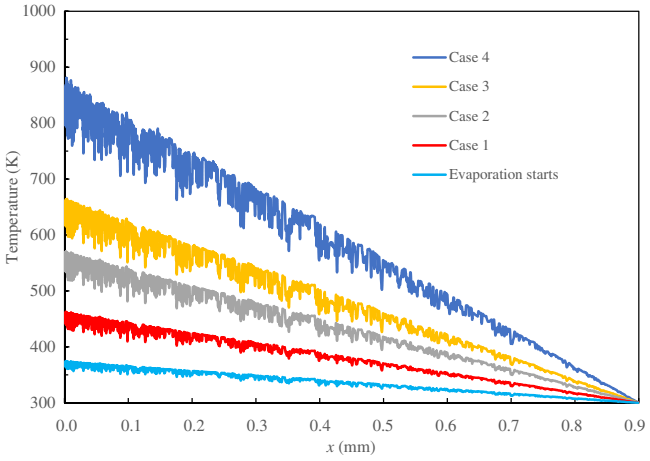

FIG. 7. Temperature profiles when evaporation starts and at the end of the pulse for each case.

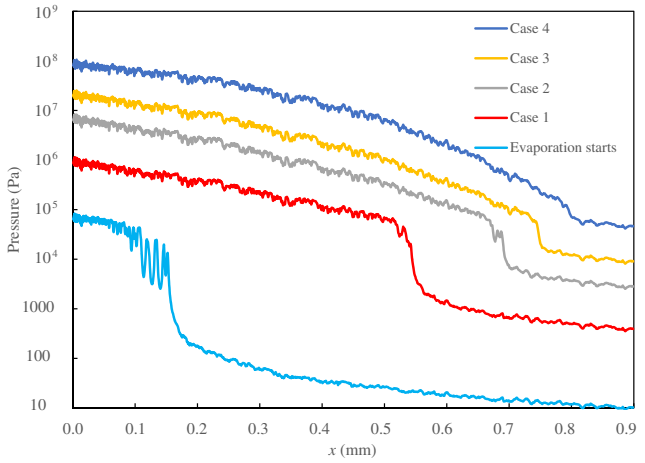

FIG. 8. Pressure profiles with logarithmic scale when evaporation starts and at the end of the pulse for each case.

higher particle velocity in the jet formation and proves the above explanation of the mechanism. It can be seen that this model not only describes the droplet expansion well, but also yields a jet at the droplet's surface with high laser energy, compared with the BI simulation.

C. Spatial profiles of temperature and pressure

During the laser pulse, the spatial profiles of temperature and pressure along the circumference of the droplet surface at the end of the pulse are shown in Figs. 7 and 8, in which the bottom curves represent the time when evaporation starts, at 4.5, 2.7, 2, and 1.2 ns in case 1–case 4 respectively.

The distributions of temperature and pressure gradually decrease from the center to the edge of the droplet surface with increasing central angle. With an increase in laser intensity, the fluctuation in temperature becomes larger, which indicates that the interface deforms more significantly under the effect of recoil pressure. The pressure

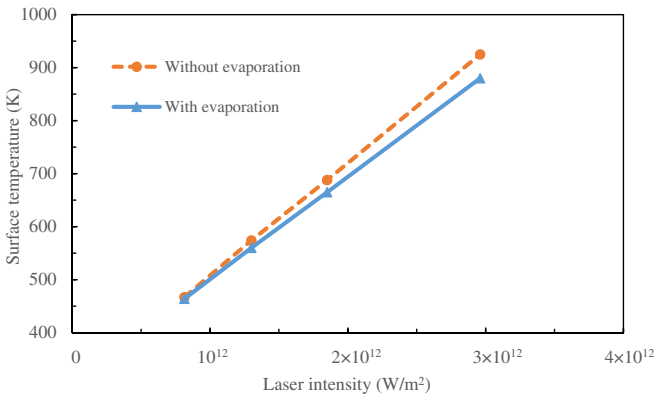

FIG. 9. Droplet-surface maximum temperature with and without considering heat taken by evaporation.

value drops sharply at a certain position, which can be considered as the turning point. With an increase in the central angle, the laser intensity decreases, and when it is lower than the threshold of evaporation, there will be no recoil pressure. Therefore, the recoil pressure does not affect the entire hemispherical surface of the droplet. According to the position of the turning point, the maximum central angles covered by recoil pressure can be obtained as follows: 65°, 75°, 79°, and 83° in case 1–case 4, respectively.

The maximum temperature at the droplet surface in the simulation and analytical solution without considering evaporation is compared in Fig. 9. As we can see, the simulation temperature considering evaporation is lower:

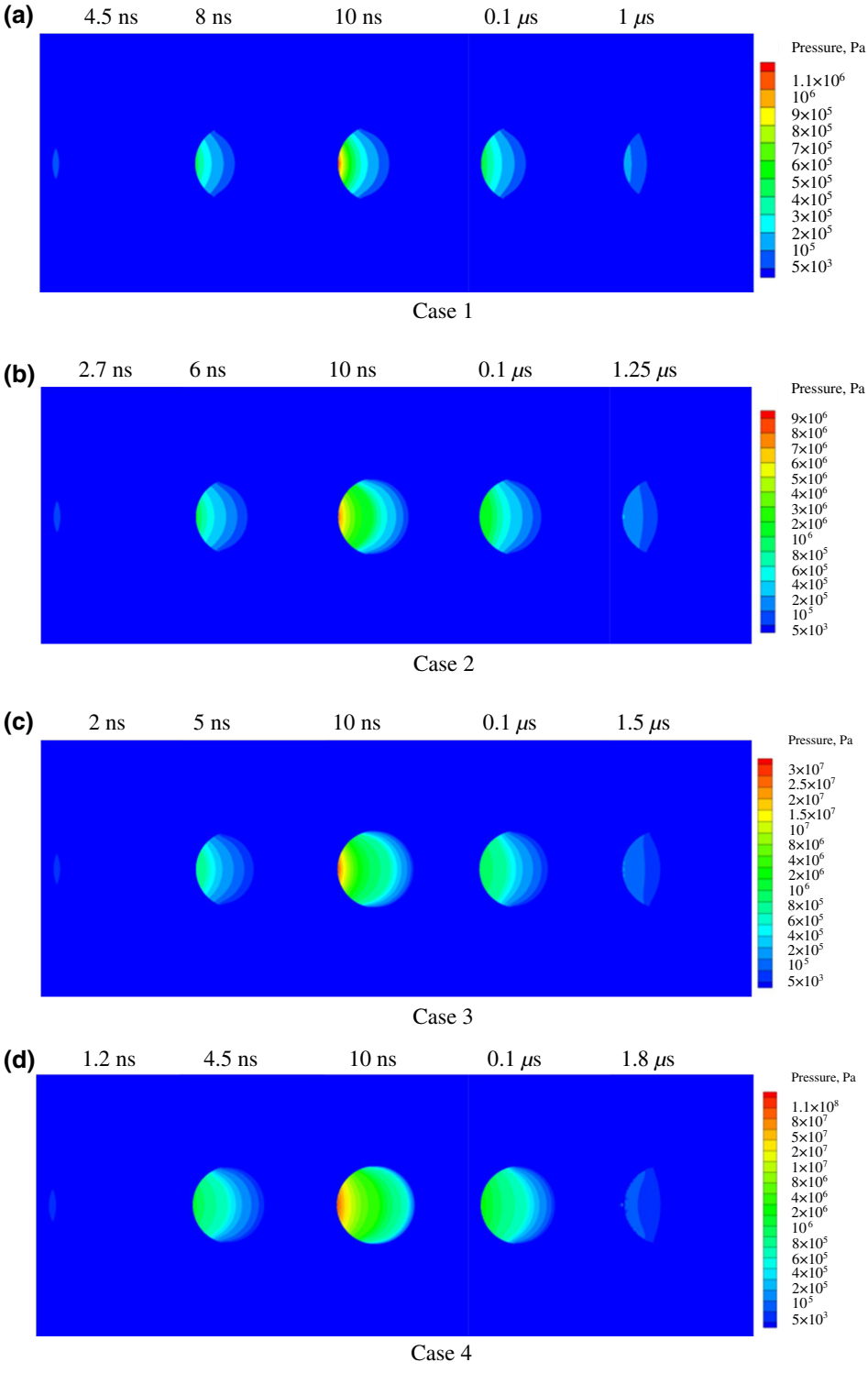

FIG. 10. Contours of pressure evolution inside water droplets during recoil impact.

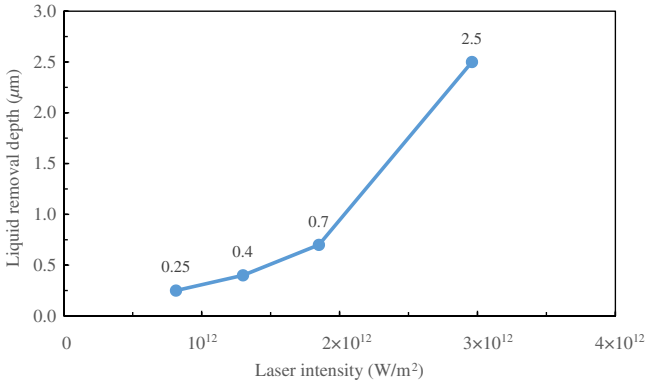

FIG. 11. Liquid-removal depths versus laser intensities.

it reaches the critical value in case 3 and exceeds it in case 4. If the liquid phase approaches the critical temperature, explosive boiling within the volume will occur, that is, phase explosion [35,36]. Although it produces a greater recoil pressure in the phase-explosion regime, the recoil pressure still becomes larger with increasing laser intensity, so it is acceptable to calculate the recoil pressure approximately with Eq. (19) when the critical temperature is exceeded. More detailed modeling in the phase-explosion regime needs to be developed and the effect on droplet deformation should be investigated in detail for future work.

The contours of pressure inside the water droplets are depicted in Fig. 10. During the impact of recoil pressure, the pressure profile propagates from left to right, and after the pulse, the pressure gradually weakens until it vanishes in 1–1.8 μs; this can be regarded as evaporation ending. As the laser energy increases, the recoil pressure becomes stronger, it will travel deeper inside the droplet, and thus, drive the droplet to become thinner.

D. Liquid-removal depth and influence of interface recession

The liquid-removal depths on the axis for different laser intensities are depicted in Fig. 11. Because the thermal-diffusion coefficient of water is small, energy will not be conducted into a deeper layer of the droplet. The liquid-removal depth is much shallower than the absorption depth, and the effect of interface recession on droplet deformation and expansion can be neglected. Although laser energy is deposited in a thin layer, it does not vaporize all liquid of this layer, but forms a superheated zone in the superficial layer, which makes surface evaporation more intense and produces a stronger recoil pressure.

IV. CONCLUSIONS

A comprehensive hydrodynamic model is established to simulate nanosecond pulsed laser ablation on a water droplet. The mechanism of droplet deformation and heat and mass transfer is mainly revealed by numerical simulations.

Droplet deformations in the simulation are consistent with experimental observations of both morphology and measured data, such as axial speed and radial expansion of the droplet. In the early stage, a crater is formed near the axis at a higher recoil pressure, which cannot be seen in the side-view images taken in the experiment. With the highest laser intensity, the droplet is propelled into a curved thin sheet and a jet flow is also simulated that is viewed similarly in the experiment. The laser energy near the axis is high, which causes the fluid to move faster from there. When the deformed droplet becomes thin enough under the impact of recoil pressure, the high-speed fluid near the axis rushes out from the opposite side to that irradiated by the laser and forms a jet. The vector fields in the deformed droplet prove the explanation of the mechanism.

It can be found from the simulation results that the surface temperature reaches and even exceeds the critical temperature with higher laser intensity. With an increase of laser energy, the central angle covered by recoil pressure becomes larger. Even with the highest laser energy, the recoil pressure does not completely cover the whole hemispherical surface of the droplet.

The liquid-removal depth is far shallower than the laser-deposition depth, and this implies that intense evaporation of this thin layer leads to deformation of the droplet under strong recoil pressure.

ACKNOWLEDGMENTS

This work is jointly supported by the National Natural Science Foundation of China under Grant No. 51776031 and the Fundamental Research Funds for the Central Universities (Grant No. DUT19LAB04).

[1] A. L. Klein, C. W. Visser, W. Bouwhuis, H. Lhuissier, C. Sun, J. H. Snoeijer, E. Villermaux, D. Lohse, and H. Gelderblom, Laser impact on a drop, Phys. Fluids **27**, 91106 (2015).

[2] Y. Kawasuji, K. Nowak, T. Hori, T. Okamoto, H. Tanaka, Y. Watanabe, T. Abe, T. Kodama, Y. Shiraishi, H. Nakarai, T. Yamazaki, S. Okazaki, T. Saito, and H. Mizoguchi, Key components technology update of the 250W high-power LPP-EUV light source, Proc. SPIE **10143**, 101432G (2017).

[3] J. Fujimoto, T. Hori, T. Yanagida, and H. Mizoguchi, Development of laser-produced tin plasma-based EUV light source technology for HVM EUV lithography, Phys. Res. Int. **2012**, 1 (2012).

[4] A. Y. Vinokhodov, M. S. Krivokorytov, Y. V. Sidelnikov, V. M. Krivtsun, V. V. E. Medvedev, and K. N. Koshelev, High brightness EUV sources based on laser plasma at using droplet liquid metal target, Quantum Electron. **46**, 473 (2016).

[5] H. Mizoguchi, K. M. Nowak, H. Nakarai, T. Abe, T. Ohta, Y. Kawasuji, H. Tanaka, Y. Watanabe, T. Hori, T. Kodama, Y. Shiraishi, T. Yanagida, T. Yamada, T. Yamazaki, S. Okazaki, and T. Saitou, Update of EUV source development status for HVM lithography, J. Laser Micro/Nanoeng. **11**, 276 (2016).

[6] D. Kurilovich, T. D. F. Pinto, F. Torretti, R. Schupp, J. Scheers, A. S. Stodolna, H. Gelderblom, K. S. E. Eikema, S. Witte, and W. Ubachs, Expansion Dynamics After Laser-Induced Cavitation in Liquid Tin Microdroplets, Phys. Rev. Appl. **10**, 054005 (2018).

[7] A. L. Klein, W. Bouwhuis, C. W. Visser, H. E. Lhuissier, C. Sun, J. H. Snoeijer, E. Villermaux, D. Lohse, and H. Gelderblom, Drop Shaping by Laser-Pulse Impact, Phys. Rev. Appl. **3**, 044018 (2015).

[8] A. L. Klein, D. Lohse, M. Versluis, and H. Gelderblom, Apparatus to control and visualize the impact of a high-energy laser pulse on a liquid target, Rev. Sci. Instrum. **88**, 95102 (2017).

[9] D. Kurilovich, A. L. Klein, F. Torretti, A. Lassise, R. Hoekstra, W. Ubachs, H. Gelderblom, and O. O. Versolato, Plasma Propulsion of a Metallic Microdroplet and its Deformation upon Laser Impact, Phys. Rev. Appl. **6**, 14018 (2016).

[10] A. L. Klein, D. Kurilovich, H. Lhuissier, O. O. Versolato, D. Lohse, E. Villermaux, and H. Gelderblom, Drop fragmentation by laser-pulse impact, J. Fluid Mech. **893**, A7 (2020).

[11] S. A. Reijers, J. H. Snoeijer, and H. Gelderblom, Droplet deformation by short laser-induced pressure pulses, J. Fluid Mech. **828**, 374 (2017).

[12] M. S. Krivokorytov, A. Y. Vinokhodov, Y. V. Sidelnikov, V. M. Krivtsun, V. O. Kompanets, A. A. Lash, K. N. Koshelev, and V. V. Medvedev, Cavitation and spallation in liquid metal droplets produced by subpicosecond pulsed laser radiation, Phys. Rev. **95**, 031101 (2017).

[13] C. A. Stan, *et al.*, Liquid explosions induced by X-ray laser pulses, Nat. Phys. **12**, 966 (2016).

[14] A. M. Gañán-Calvo, Scaling Laws of an Exploding Liquid Column Under an Intense Ultrashort X-Ray Pulse, Phys. Rev. Lett. **123**, 64501 (2019).

[15] Z. Gao, P. Jiang, G. Mi, L. Cao, and W. Liu, Investigation on the weld bead profile transformation with the keyhole and molten pool dynamic behavior simulation in high power laser welding, Int. J. Heat Mass Transfer **116**, 1304 (2018).

[16] C. Panwisawas, C. Qiu, M. J. Anderson, Y. Sovani, R. P. Turner, M. M. Attallah, J. W. Brooks, and H. C. Basoalto, Mesoscale modelling of selective laser melting: Thermal fluid dynamics and microstructural evolution, Comput. Mater. Sci. **126**, 479 (2017).

[17] C. Sawyer, K. Iyer, X. Zhu, M. Kelly, D. Luke, and D. Amdahl, Two-dimensional laser-induced thermal ablation modeling with integrated melt flow and vapor dynamics, J. Laser Appl. **29**, 22212 (2017).

[18] Y. Ai, P. Jiang, C. Wang, G. Mi, and S. Geng, Experimental and numerical analysis of molten pool and keyhole profile during high-power deep-penetration laser welding, Int. J. Heat Mass Transfer **126**, 779 (2018).

[19] Y. Zhang, Z. Shen, and X. Ni, Modeling and simulation on long pulse laser drilling processing, Int. J. Heat Mass Transfer **73**, 429 (2014).

[20] H. Gelderblom, H. Lhuissier, A. L. Klein, W. Bouwhuis, D. Lohse, E. Villermaux, and J. H. Snoeijer, Drop deformation by laser-pulse impact, J. Fluid Mech. **794**, 676 (2016).

[21] I. A. Roberts, C. J. Wang, R. Esterlein, M. Stanford, and D. J. Mynors, A three-dimensional finite element analysis of the temperature field during laser melting of metal powders in additive layer manufacturing, Int. J. Mach. Tools Manuf. **49**, 916 (2009).

[22] S. Bag, A. Trivedi, and A. De, Development of a finite element based heat transfer model for conduction mode laser spot welding process using an adaptive volumetric heat source, Int. J. Therm. Sci. **48**, 1923 (2009).

[23] S. Torii and W. Yang, Heat transfer mechanisms in thin film with laser heat source, Int. J. Heat Mass Transfer **48**, 537 (2005).

[24] C. R. Kharangate and I. Mudawar, Review of computational studies on boiling and condensation, Int. J. Heat Mass Transfer **108**, 1164 (2017).

[25] Y. Tsui, C. Liu, and S. Lin, Coupled level-set and volume-of-fluid method for two-phase flow calculations, Numer. Heat Transfer, Part B **71**, 173 (2017).

[26] V. R. Gopala and B. G. M. van Wachem, Volume of fluid methods for immiscible-fluid and free-surface flows, Chem. – Eng. J. **141**, 204 (2008).

[27] B. M. Ningegowda and B. Premachandran, A coupled level Set and volume of fluid method with multi-directional advection algorithms for two-phase flows with and without phase change, Int. J. Heat Mass Transfer **79**, 532 (2014).

[28] N. Kumar Singh and B. Premachandran, A coupled level set and volume of fluid method on unstructured grids for the direct numerical simulations of two-phase flows including phase change, Int. J. Heat Mass Transfer **122**, 182 (2018).

[29] B. A. Nichita, I. Zun, and J. R. Thome, A level Set method coupled With a volume of fluid method for modeling of Gas-liquid interface in bubbly flow, J. Fluids Eng. **132**, 81302 (2010).

[30] D. Zhang, X. Tan, Z. Li, G. Li, and L. Li, Thermal regime and effect studying on the ablation process of thin films prepared by nanosecond pulsed laser, Phys. B **357**, 348 (2005).

[31] A. H. Persad and C. A. Ward, Expressions for the evaporation and condensation coefficients in the hertz-knudsen relation, Chem. Rev. **116**, 7727 (2016).

[32] C. Panwisawas, Y. Sovani, R. P. Turner, J. W. Brooks, H. C. Basoalto, and I. Choquet, Modelling of thermal fluid dynamics for fusion welding, J. Mater. Process. Technol. **252**, 176 (2018).

[33] E. R. Likhachev, Dependence of water viscosity on temperature and pressure, Tech. Phys. **48**, 514 (2003).

[34] N. B. Vargaftik, B. N. Volkov, and L. D. Voljak, International tables of the surface tension of water, J. Phys. Chem. Ref. Data **12**, 817 (1983).

[35] S. Reich, P. Schönfeld, P. Wagener, A. Letzel, S. Ibrahimkutty, B. Gökce, S. Barcikowski, A. Menzel, T. Dos Santos Rolo, and A. Plech, Pulsed laser ablation in liquids: Impact of the bubble dynamics on particle formation, J. Colloid Interface Sci. **489**, 106 (2017).

[36] N. M. Bulgakova and A. V. Bulgakov, Pulsed laser ablation of solids: Transition from normal vaporization to phase explosion, Appl. Phys. A: Mater. Sci. Process. **73**, 199 (2001).